O(3) are the bond strength sums not very close to 2 v.u. The oxygen atoms O(5) to O(15) exhibit a slight deviation below the theoretical value for the hydroxyls and above that for the water molecules.

The study of the thermal dehydration of aluminite (Basset & Goodwin, 1949) shows that when the mineral is heated to constant weight at 100–115 °C, the weight loss is about 21%. This corresponds closely to the loss of all the free water molecules simultaneously. Therefore the behaviour of all the free water molecules is the same in spite of the fact that O(14) is not directly H-bonded to any polyhedron, unlike O(12), O(13) and O(15).

As already mentioned in the *Introduction*, aluminite was probably crystallized from weakly acidic solutions. The formation of condensed cations is known to occur in aluminium solution as neutrality is approached from the acid side. The presence of the hydroxy-aluminium cation in the aluminite structure confirms the hypothesis concerning the crystallization environment of this mineral and suggests also that the structures of the other members of the basic aluminium sulphate group are characterized by similar polynuclear cations.

This work was supported by the Consiglio Nazionale delle Ricerche, Centro di Studio per la Mineralogia e la Geochimica dei Sedimenti, Firenze, Italy.

### References

Basset, H. & Goodwin, T. H. (1949). *J. Chem. Soc.* pp. 2239–2279.

Baur, W. H. (1964). *Acta Cryst.* **17**, 1361–1369.

Brown, I. D. (1976). *Acta Cryst.* A**32**, 24–31.

Brown, I. D. & Shannon, R. D. (1973). *Acta Cryst.* A**29**, 266–282.

Dent Glasser, L. S. (1971). *Trans. Br. Ceram. Soc.* **70**, 167–169.

Dent Glasser, L. S. & Giovanoli, R. (1970). *Chimia*, **24**, 344–345.

Dent Glasser, L. S. & Giovanoli, R. (1972). *Acta Cryst.* B**28**, 519–524.

Donnay, G. & Donnay, J. D. H. (1973). *Acta Cryst.* B**29**, 1417–1425.

Frondel, C. (1968). *Am. Mineral.* **53**, 717–721.

Germain, G., Main, P. & Woolfson, M. M. (1971). *Acta Cryst.* A**27**, 368–376.

Hollingworth, M. A. & Bannister, M. A. (1950). *Mineral. Mag.* **29**, 1–17.

*International Tables for X-ray Crystallography* (1974). Vol. IV. Birmingham: Kynoch Press.

Menchetti, S. & Sabelli, C. (1974). *Tschermaks Mineral. Petrogr. Mitt.* **21**, 164–178.

Menchetti, S. & Sabelli, C. (1976). *Mineral. Mag.* **40**, 599–608.

Palache, C., Berman, H. & Frondel, C. (1951). *Dana's System of Mineralogy*, Vol. 2. New York: John Wiley.

Stewart, R. F., Davidson, E. R. & Simpson, W. T. (1965). *J. Chem. Phys.* **42**, 3175–3187.

---

*Acta Cryst.* (1978). B**34**, 2412–2424

# High-Temperature Intergrowth Structures in the $Fe_2O_3$–$TiO_2$ System – Metal Atom Ordering in the Intergrowth Boundaries

By I. E. Grey

*CSIRO Division of Mineral Chemistry, PO Box* 124, *Port Melbourne, Victoria* 3207, *Australia*

and L. A. Bursill

*Physics Department, University of Melbourne, Parkville, Victoria* 3052, *Australia*

(*Received* 1 *November* 1977; *accepted* 6 *January* 1978)

In the $Fe_2O_3$–$TiO_2$ system, at temperatures below about 1450 °C, the composition range 8–16 wt% $Fe_2O_3$ is spanned by a continuous series of $(121)_r$–$(132)_r$ rutile crystallographic shear (CS) structures. Above 1450°C they undergo a reversible transformation to intergrowth structures in which rutile slabs are periodically displaced by $\frac{1}{2}[0\bar{1}1]_r$ across $(0kl)_r$ boundaries. With different $Fe_2O_3$ contents, the orientation of these boundaries varies between $(020)_r$ and $(031)_r$. Here is reported an analysis of the metal atom ordering within the $(0kl)_r$ boundaries using electron diffraction/microscopy and single-crystal X-ray diffraction techniques. It is found that the boundaries are actually slabs, with widths ranging from about 4·5 to 9 Å, within which elements of rutile and corundum structures form coherent intergrowths, parallel to $(101)_r$. The structures are metastable at low temperatures and decompose under electron-beam heating to give the component oxides, haematite and rutile. Structural relations with the ferric titanate mineral pseudorutile are discussed and a mechanism for the low–high-temperature structure transformation is suggested.

## 1. Introduction

In their study on the $Cr_2O_3$–$TiO_2$ system, Flörke & Lee (1970) reported that the Andersson phases $Cr_2Ti_{n-2}O_{2n-1}$, $n = 8$–$12$, transformed reversibly into high modifications above 1400 °C. The low-temperature Andersson phases may be described as crystallographic shear (CS) phases derived from rutile by the CS operation $\{121\}_r\,\frac{1}{2}\langle 0\bar{1}1\rangle_r$ (Andersson, Sundholm & Magnéli, 1959). Flörke & Lee (1970) did not establish the structures of the high-temperature modifications, but noted that above the transformation temperature, the powder X-ray diffractograms remained similar to those for the low-temperature precursors, but were simplified because of the disappearance of many lines.

We have recently reported the observation of similar behaviour in the $Fe_2O_3$–$TiO_2$ system for compositions in the range 8–16 wt% $Fe_2O_3$ (Bursill, 1974; Bursill, Grey & Lloyd, 1976). In this system, members of the $(121)_r$–$(132)_r$ families of rutile-derived 'swinging-shear' structures transform to high-temperature modifications above 1450 °C. From a combined electron diffraction–single-crystal X-ray diffraction study we established the structural principles for the high-temperature phases whereby the structures may be described as consisting of rutile slabs which are periodically displaced relative to one another by the vector $\frac{1}{2}[0\bar{1}1]_r$ at boundaries parallel to $(0kl)_r$. Compositional variations in the system are accommodated both by variations in the separation between the displacement boundaries and their orientation. The observed indices of the boundaries are all contained in the $[100]_r$ zone and lie between $(031)_r$, for low iron concentrations, and $(020)_r$. We carried out a single-crystal structure analysis on a $(020)_r$ homologue which established the gross structural features, *i.e.* the orientation and separation of the displacement boundaries and the displacement vector at the boundary. However, we were unable to establish the type of metal atom ordering at the boundary. We observed some very weak superlattice reflections in the electron diffraction patterns which were attributed to metal atom ordering of the displacement boundaries. These reflections were very diffuse and elongated perpendicular to $(020)_r$, suggesting a lack of correlation of the metal ordering between adjacent boundaries. In this paper we present structural models for the metal ordering which were deduced from the observed diffraction effects.

## 2. Experimental

Details of sample preparation in the $Fe_2O_3$–$TiO_2$ system are given in the earlier references (Bursill, 1974; Bursill, Grey & Lloyd, 1976). The samples were examined by transmission electron microscopy and single-crystal X-ray diffraction, using the precession method. The electron-microscopy studies were performed with JEM-7 and JEOL-100C transmission electron microscopes fitted with goniometer stages. Thin fracture fragments of the samples were obtained by crushing and were dispersed on carbon support films for examination.

## 3. Observations

### 3.1. *Electron diffraction*

Electron diffraction patterns for high-temperature modifications in the $Fe_2O_3$–$TiO_2$ system have been given in Fig. 1 of Bursill, Grey & Lloyd (1976). With changes in $Fe_2O_3$ content and preparation temperature, the directions of the superlattice rows were observed to vary between $\mathbf{g}(031)_r$ and $\mathbf{g}(020)_r$. $[100]_r$ zone axis patterns were thus used to characterize the orientation and separation of the displacement boundaries. In addition to the strong sharp diffraction spots displayed in simple zone axis patterns such as $[100]_r$ and $[001]_r$, we also observed weak diffuse diffraction effects when the crystals were tilted away from these zones.

Examples of the diffuse scattering are shown in Figs. 1 and 2 and the general features may be summarized as follows. (i) The diffuse scattering is in the form of streaks, *i.e.* lines of diffuse intensity. (ii) The orientation of the streaks is always in the direction of the superlattice rows, *i.e.* in directions between $\mathbf{g}(031)_r$ and $\mathbf{g}(020)_r$. All $(0kl)_r$, $l$ non-zero, structures were observed to be twinned and pairs of intersecting diffuse streaks occurred parallel to $\mathbf{g}(0kl)_r$ and $\mathbf{g}(0k\bar{l})_r$, Fig. 1(*c*) and (*d*). (iii) The diffuse streaks intersect $(h0l)_r$ reciprocal-lattice sections at relatively sharp spots which form a superlattice directed along $\mathbf{g}(101)_r$ (Fig. 2*a*). A second set of spots was often observed along $\mathbf{g}(10\bar{1})_r$, indicating a twin orientation. (iv) The diffuse superlattice reflections were confined to pairs of spots only, about the rutile subcell reflections. Furthermore, these reflections were associated only with subcell reflections with $h_r$, $l_r = 2n + 1$ in the $(h0l)_r$ section. (v) The periodicity along $\mathbf{g}(101)_r$ of the diffuse reflections was observed to be related to the superlattice orientation, $\mathbf{g}(0kl)_r$, such that a periodicity close to $5d(101)_r$ was found for the $(020)_r$ superstructures and this decreased towards $4d(101)_r$ as the orientation of the superlattice swung towards $(031)_r$. (vi) Upon prolonged exposure to the electron beam, the intensities of the diffuse superlattice reflections gradually weakened, and a new set of reflections appeared along $\mathbf{g}(101)_r$ with a periodicity of $3d(101)_r$. Eventually, the original diffuse reflections disappeared completely, leaving only the $3d(101)_r$ reflections. These also occur in twinned orientations along $\mathbf{g}(101)_r$ and $\mathbf{g}(10\bar{1})_r$. Note that this latter pattern,

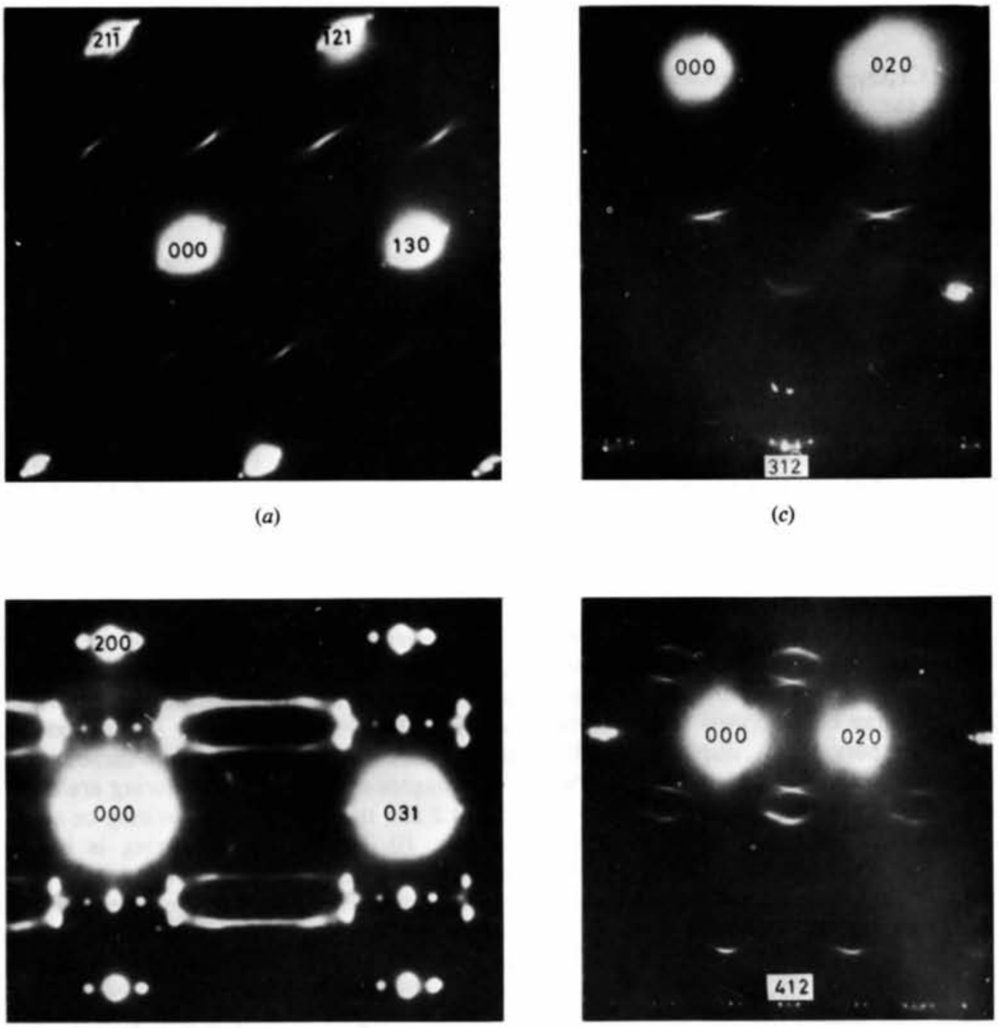

(a) (c)

(b) (d)

Fig. 1. Electron diffraction patterns for $(0kl)_r$ superstructures showing diffuse streaking.

Fig. 2(*d*), is identical with that for twinned corundum when viewed down $[100]_{cor}$. The sequence of changes in the $(h0l)_r$ pattern induced by beam heating is shown in Fig. 2(*a*)–(*d*). (vii) High-resolution lattice images of the high-temperature structures were obtained using superlattice reflections in the $[10\bar{1}]_r$ zone. An example is shown in Fig. 3, for a CS orientation close to $(020)_r$. 4·6 Å fringes corresponding to the $b_r$ axial repeat for the rutile slabs are resolved in some places. The CS 'planes' are parallel to $(020)_r$ over lengths of only 100 to 150 Å. In fact the 'planes' show correlated oscillating behaviour across rather ill-defined planes roughly perpendicular to $(020)_r$. These latter planes may be remnants of the $(002)_r$ twin boundaries observed in the low-temperature precursors. The most important observation from Fig. 3 is that the CS 'planes' are in fact slabs, with thicknesses of 9·2 Å in places, *i.e.* $2b_r$, although the width appears to be 4·6 Å (*i.e.* $b_r$) over most of their length. Fig. 3(*b*) and (*c*) show enlarged areas of Fig. 3(*a*) and indicate regular intergrowth of several spacings along the length of the slabs. The mean spacing of 11·5 Å is the same as the $4{\cdot}6d(101)_r$ periodicity observed on the electron diffraction pattern. (viii) Fig. 4(*a*) shows a high-resolution image, again viewed down $[10\bar{1}]_r$, of an $(020)_r$ CS structure after prolonged beam heating, *i.e.* the image was obtained from a corundum-like diffraction pattern similar to that shown in Fig. 4(*b*). Instead of the continuous CS slabs shown in Fig. 3, much wider, lens-like blocks are now observed, still aligned approximately along $\mathbf{g}(020)_r$.

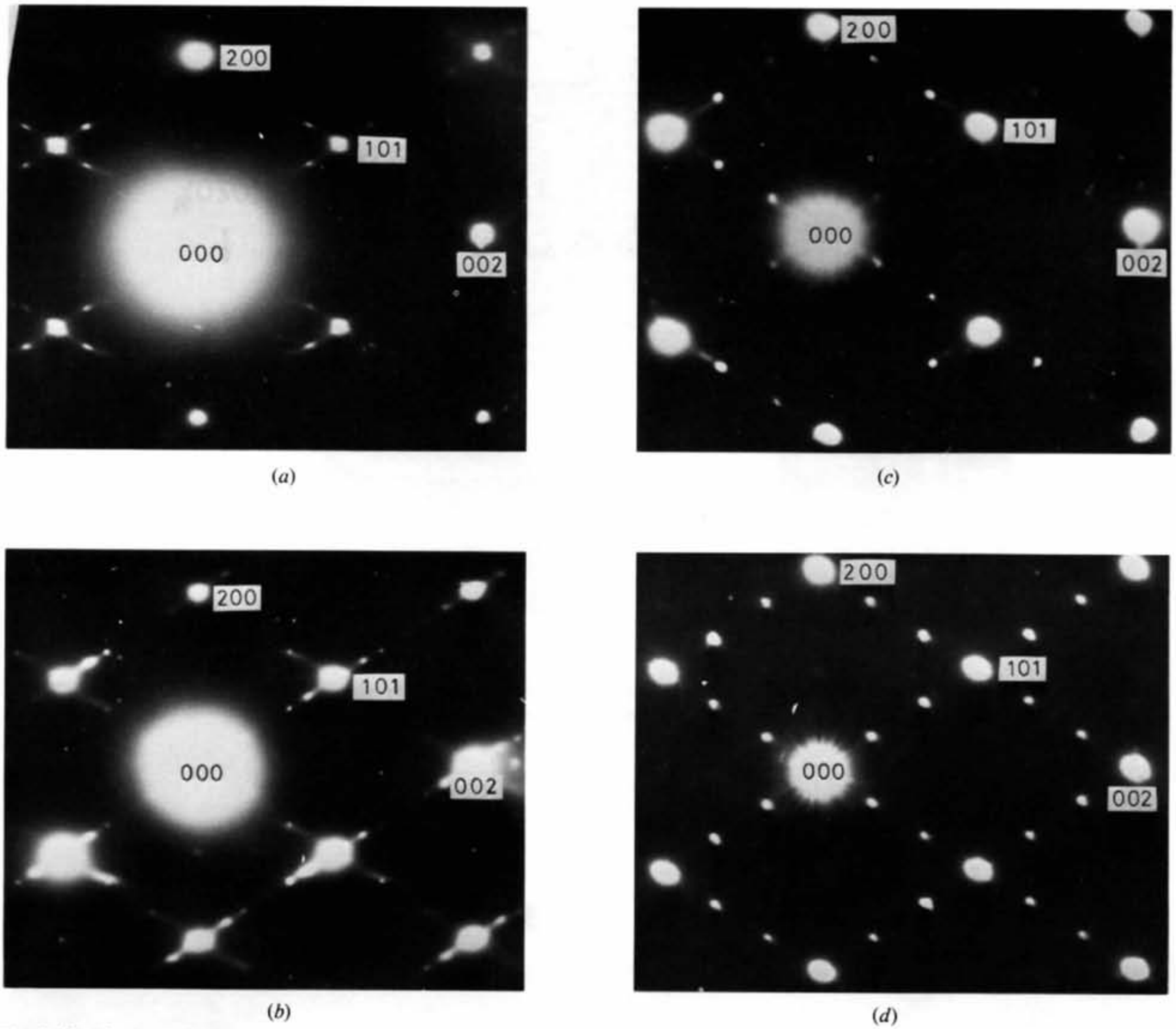

Fig. 2. $[010]_r$ zone axis electron diffraction patterns for an $(0kl)_r$ superstructure. The diffuse streaks, shown in Fig. 1, intersect this section as relatively sharp spots, forming a superlattice along $\mathbf{g}(101)_r$ with a periodicity of $\sim 5d(101)_r$. The sequence $(a) \rightarrow (d)$ shows the effect of electron-beam heating; the $5d(101)_r$ superlattice spots gradually disappear and are replaced by superlattice spots with a $3d(101)_r$ periodicity.

The lenses contain fringes with 7·2 Å separation $= 3d(101)_r$. Their length varies between about 50 and 500 Å and their width ranges up to 30 Å. The 4·6 Å rutile fringes are clearly visible, parallel to $(020)_r$.

### 3.2. *Single-crystal X-ray diffraction studies*

A number of crystals selected from high-temperature preparations in the $Fe_2O_3$–$TiO_2$ system were studied using the precession method. This proved a useful procedure complementing the electron diffraction studies and offering some distinct advantages. In particular, it was possible to orient selected crystals so that *any* desired reciprocal-lattice section could be obtained (remounting the crystal when necessary). Alternatively, a reciprocal-lattice vector could be set as the horizontal axis and reciprocal sections could be obtained for 360° rotation about this axis. This proved useful in mapping the diffuse scattering, when the CS vector, $\mathbf{g}(0kl)_r$, was taken as the horizontal axis. Furthermore, upper-level reciprocal sections could be obtained, giving information on systematic extinctions as well as reliable estimates of the intensities of the diffuse reflections.

Typical precession photographs are shown in Fig. 5 for an $(020)_r$ CS structure. Fig. 5(*a*) exhibits diffuse streaks parallel to $\mathbf{g}(020)_r$. Assuming that these streaks result from metal atom ordering within the $(020)_r$

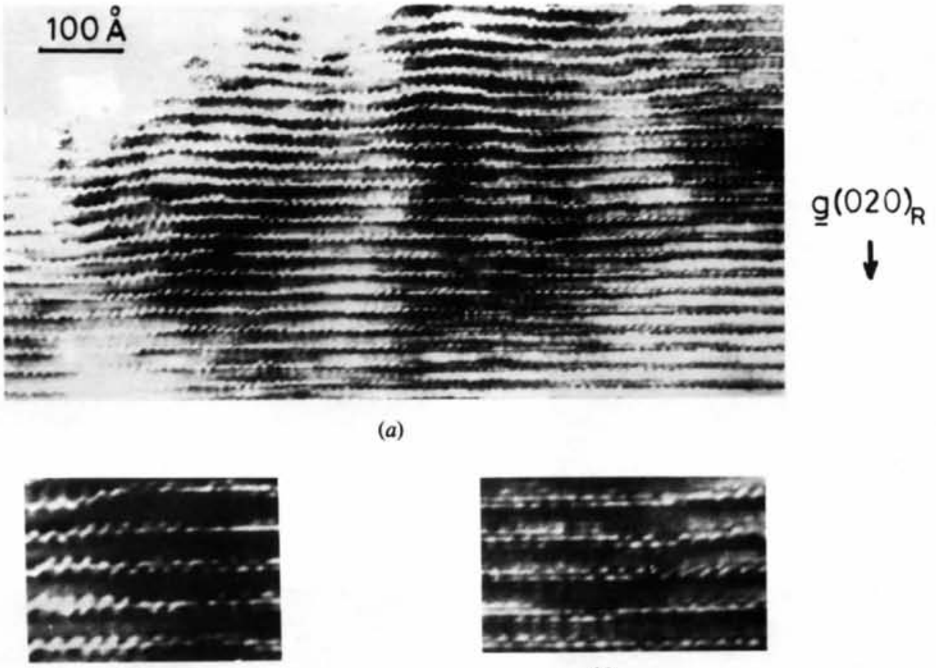

(a)

(b)

(c)

Fig. 3. High-resolution electron micrograph of an $(020)_r$ high-temperature intergrowth structure, viewed along $[10\bar{1}]_r$. Selected areas on Fig. 3(*a*) are magnified in Fig. 3(*b*) and (*c*) respectively to show the projected charge-density detail within the $(020)_r$ boundaries. Between the boundaries, 4·6 Å rutile fringes are resolved in some areas.

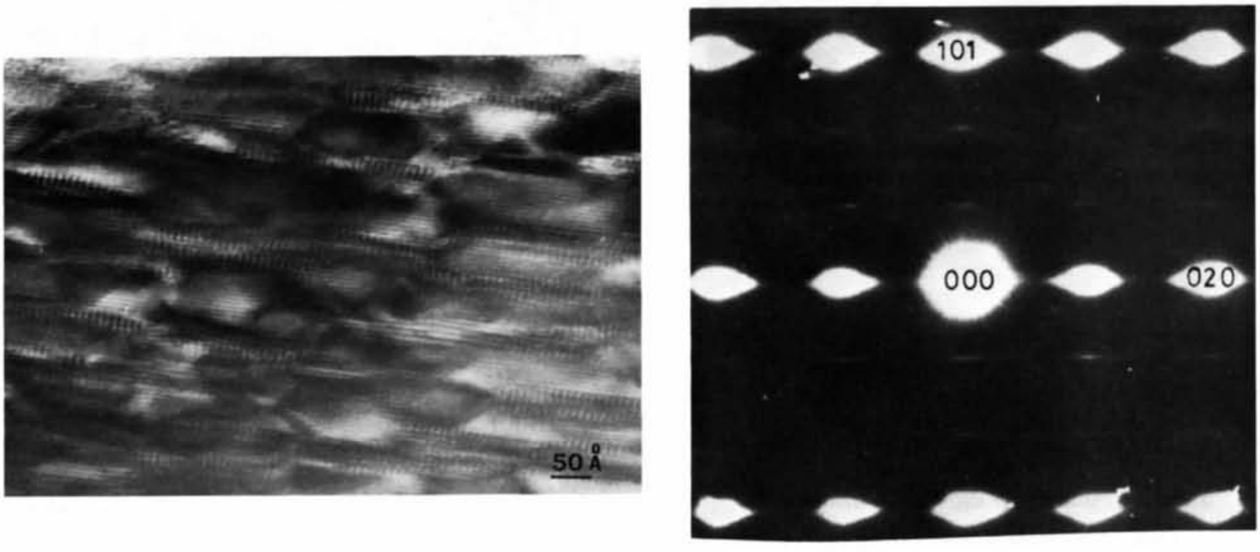

(a)

(b)

Fig. 4. High-resolution electron micrograph of an $(020)_r$ intergrowth structure subjected to prolonged electron-beam heating. The structure is viewed down $[10\bar{1}]_r$ in (*a*) and the diffraction pattern used to image the structure is shown in (*b*). The structure has broken down to give lenses of haematite showing $3d(101)_r$ fringes, still aligned approximately along $(020)_r$ in a rutile matrix. 4·6 Å fringes $\equiv b_r$ are resolved in the rutile segments.

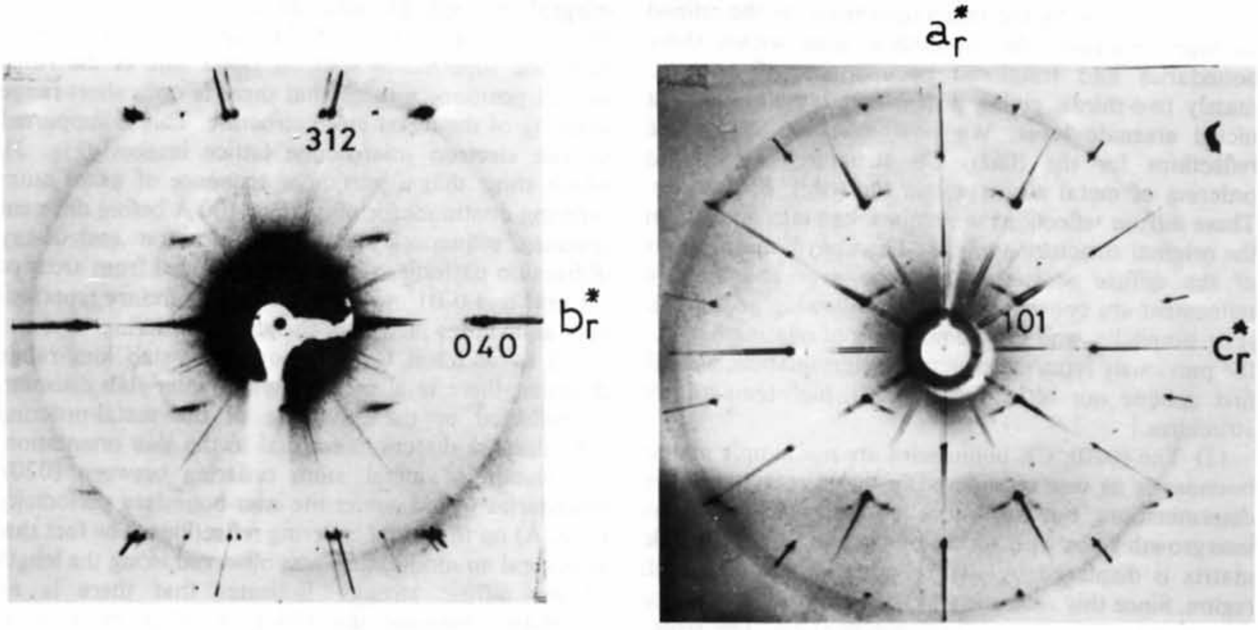

(*a*) (*b*)

Fig. 5. X-ray precession photographs of an $(020)_r$ intergrowth structure. (*a*) Reciprocal-lattice section with $b_r^*$ as horizontal axis, showing diffuse streaks parallel to $\mathbf{g}(020)_r$. (*b*) $[010]_r$ zone axis pattern for an $(020)_r$ intergrowth structure. The diffuse streaks shown in Fig. 5(*a*) intersect this section as relatively sharp spots, indicating a superlattice along $\mathbf{g}(101)_r$. Superlattice reflections also occur along $\mathbf{g}(10\bar{1})_r$, in twin orientation.

boundaries, a measure of the boundary thickness may be obtained by taking the reciprocal of the length of the streak. Measurements of the streak length on various photographs yielded boundary widths of 4·5 to 9 Å, corresponding to between two and four metal atom layers parallel to $(020)_r$, in agreement with the width deduced from Fig. 3.

An $[010]_r$ zone axis section is shown in Fig. 5(*b*). The diffuse streaks intersect this section at relatively sharp spots, forming superlattices along $\mathbf{g}(101)_r$ and $\mathbf{g}(10\bar{1})_r$. However, whereas the electron diffraction patterns showed pairs of superlattice spots of comparable intensity about each subcell position, the X-ray precession patterns show highly asymmetric intensity distributions; in many cases, only one of the pair of spots is discernible. The intensity of the strongest diffuse reflections was about one hundredth of that of the strongest rutile subcell reflections. Precession photographs showing diffuse scattering as in Fig. 5 generally required exposure times of the order of 100 h or more.

In general there was no modulation of intensity along the diffuse streaks and in all specimens studied the maxima of the streaks appeared to lie in $[010]_r$ sections. Considering then the centres of the streaks as Bragg reflections, the diffuse scattering from the samples studied could be described in each case by a monoclinic unit cell with $a = a_r - c_r$, $b = b_r$, $c = \delta c_r$, $\beta = [001]_r \wedge [10\bar{1}]_r = 123 \cdot 5°$, where $\delta$ was observed to take non-integral values between 4 and 5, for the different samples. The only systematic extinction common to all samples studied was $hkl$, $h + k = 2n + 1$, giving a *C*-centred monoclinic cell.

## 4. Structural models for metal atom ordering

### 4.1. *General structural features*

We have previously reported the determination of the average structure of an $(020)_r$ CS structure (Bursill, Grey & Lloyd, 1976). The model, in orthorhombic space group $A2_1am$, had unit-cell vectors $a = a_r$ (4·62 Å), $b = 11b_r$ (51·36 Å) and $c = c_r$ (2·95 Å). It comprised rutile slabs, infinitely extended along $(020)_r$ but displaced relative to one another by $\frac{1}{2}[0\bar{1}1]_r$ across $(020)_r$ planar boundaries. The interboundary separation was 25·7 Å. A satisfactory refinement to the X-ray intensity data was obtained, but it was not possible to determine the metal atom ordering within the $(020)_r$ boundaries. This was because the unit cell was defined only by the sharp reflections. In the refined average structure, the octahedral sites within these boundaries had fractional occupancies of approximately two-thirds, giving a disordered, metal-deficient nickel arsenide layer. We now interpret the diffuse reflections for the $(0kl)_r$ CS structures as due to ordering of metal atoms within the $(0kl)_r$ boundaries. These diffuse reflections were not taken into account in the original structure analysis. The above observations of the diffuse scattering and the average structure refinement are consistent with the following postulates. [For simplicity, and for the purposes of relating back to the previously reported structure determination, we will first confine our attention to $(020)_r$ high-temperature structures.]

(1) The $(020)_r$ CS boundaries are not simple planar boundaries as was considered in the average structure determination, but are more correctly described as intergrowth slabs with widths of 4·5 and 9 Å. The rutile matrix is displaced by $\frac{1}{2}[0\bar{1}1]_r$ across the intergrowth region. Since this vector is an O—O vector, the O lattice is continuous across the intergrowth slabs. The structure refinement for the $11(020)_r$ structure confirmed this continuous nature of the anion lattice, and revealed that at the boundaries, the 'puckered' $(100)_r$ O layers of rutile are flattened to give segments of almost perfect hexagonal close packing.

(2) Within the intergrowth slabs, the metal atom site occupations (and, presumably, displacements) undergo periodic variations parallel to $(101)_r$ planes, with repeat distances, of $4\text{–}5d(101)_r$. The observation of non-integral 'average' periodicities along $g(101)_r$ as well as the very limited extent of the superlattice rows, with only one superlattice spot on either side of the rutile subcell positions implies that there is only short-range ordering of the metal atom structure. This is supported by the electron microscope lattice images (Fig. 3), which show that a particular sequence of metal atom ordering continues for only 50 to 100 Å before different ordering sequences occur. The electron and X-ray diffraction patterns, which were obtained from areas of ~1 $\mu m^2$ and 0·01 $mm^2$ respectively, therefore represent only an average picture of the atomic ordering.

(3) In addition to the above intra-slab long-range disorder, there is also considerable inter-slab disorder, as reflected in the streaking of the metal-ordering reflections in directions normal to the slab orientation. Correlation of metal atom ordering between $(020)_r$ boundaries would confer the inter-boundary periodicity (~26 Å) on the metal-ordering reflections. The fact that in general *no* modulation was observed along the length of the diffuse streaks indicates that there is no correlation between the $(101)_r$ metal atom arrangements in successive $(020)_r$ slabs. Individual $(020)_r$ intergrowth slabs thus diffract independently of one another, and the centres of the streaks may be considered to represent the Bragg reflections of a unit cell defined by the intra-slab metal atom ordering. As pointed out in § 3.2, the unit cells thus determined for different $Fe_2O_3$–$TiO_2$ compositions were all *C*-centred monoclinic with $a = a_r - c_r$, $b = b_r$, $c = \delta c_r$ with $\delta$ in the range 4–5, $\beta = 123{\cdot}5°$. Using these unit cells, and the observed

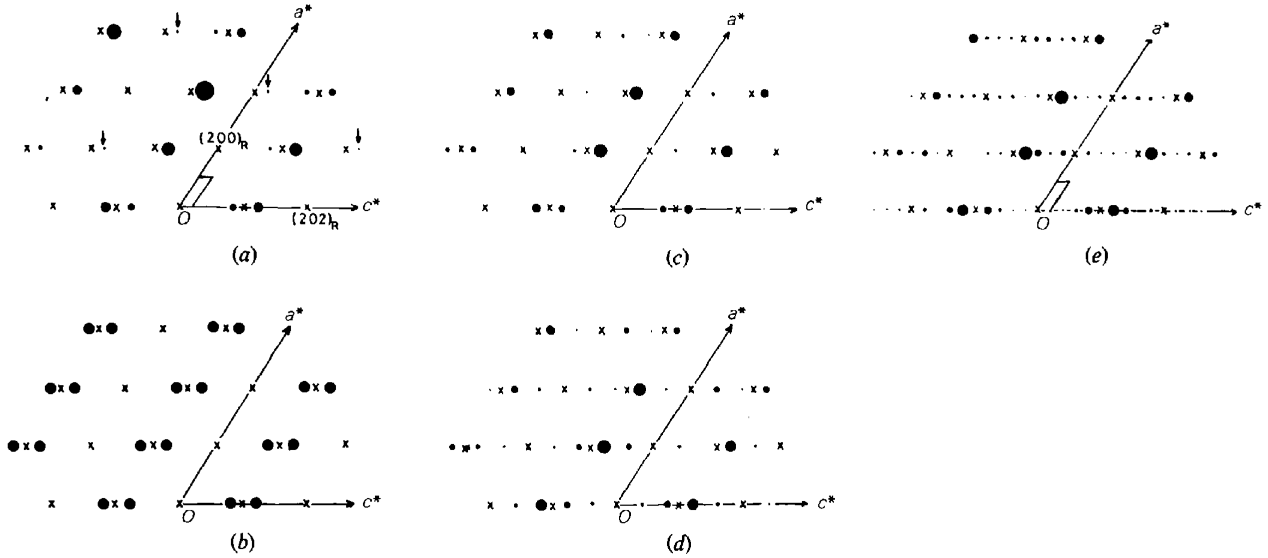

Fig. 6. (*a*) Observed and (*b*)–(*e*) calculated (*h*0*l*) X-ray diffraction patterns for different $(101)_r$ metal atom ordering models. The intensity results are presented as filled circles of area $F^2$. The observed intensities in (*a*) were converted to $F^2$ values by applying Lp corrections. Calculated patterns are for (*b*) models I and II – sinusoidal with ideal coordinates, (*c*) model I – sinusoidal with adjustment to coordinates for metal atom repulsions, (*d*) model $I_{ord}$ – with repulsion and (*e*) model $II_{ord}$ – with repulsion. See Table 1 for model parameters. Metal atoms only were considered in the calculations.

Table 1. *Metal atom parameters for sinusoidal modulation and ordered models*

Monoclinic unit cell, $a = 5{\cdot}46$, $b = 4{\cdot}67$, $c = 15{\cdot}08$ Å, $\beta = 123{\cdot}5°$.

| | $M(1)$ | | | | $M(2)$ | | | | $M(3)$ | | | |
|---|---|---|---|---|---|---|---|---|---|---|---|---|
| | $x$ | $y$ | $z$ | Occupancy | $x$ | $y$ | $z$ | Occupancy | $x$ | $y$ | $z$ | Occupancy |
| Model I – IDEAL | 0·0 | 0·0 | 0·0 | 1·0 | 0·00 | 0·0 | 0·40 | 0·28 | 0·00 | 0·0 | 0·20 | 0·72 |
| Model II – IDEAL | 0·0 | 0·0 | 0·0 | 0·28 | 0·00 | 0·0 | 0·40 | 0·90 | 0·00 | 0·0 | 0·20 | 0·46 |
| Model I + REPULSION | 0·0 | 0·0 | 0·0 | 1·0 | 0·957 | 0·0 | 0·397 | 0·28 | 0·546 | 0·0 | 0·200 | 0·72 |
| Model $I_{ord}$ + REPULSION | 0·0 | 0·0 | 0·0 | 1·0 | | — | | 0 | 0·546 | 0·0 | 0·200 | 1·0 |
| Model $II_{ord}$ + REPULSION | 0·975 | 0·0 | 0·101 | 1·0 | 0·930 | 0·0 | 0·288 | 1·0 | 0·530 | 0·0 | 0·400 | 1·0 |

intensity distribution of the diffuse reflections, we now derive possible models for the intra-slab metal ordering. We first consider infinitely extending three-dimensional structural models and then consider how slabs of finite width normal to $(020)_r$ can form coherent intergrowths with rutile, maintaining displacement vector $\frac{1}{2}[0\bar{1}1]_r$ across the $(020)_r$ slabs to build up complete models for the $(020)_r$ intergrowth phases. The extension of these principles to the swinging $(0kl)_r$ structures follows naturally.

### 4.2. *Sinusoidal variation of metal atom site occupancies*

An $[010]_r$ zone axis precession photograph of an $(020)_r$ structure (*e.g.* Fig. 5*b*) is reproduced diagrammatically in Fig. 6(*a*). Only one set of the twinned superlattice reflections is shown. The relative intensities (corrected for Lorentz–polarization, to give $F^2$) of the superlattice reflections are represented by the areas of the filled circles. Reflections due to the rutile subcell are marked with crosses. The intergrowth structure represented in Fig. 6(*a*) has $c = 5c_r$. This periodicity was commonly observed in the diffraction patterns for $(020)_r$ structures. Except for a few extremely weak spots, marked with arrows in Fig. 6(*a*), the indices of the observed diffuse reflections on the zero and upper levels all conformed to an $F$-centring extinction requirement and we will initially consider models in this approximation. As only one observable superlattice reflection occurs on either side of the rutile subcell positions, it follows that a sinusoidal modulation of scattering power should describe the gross features of the observed intensity distribution. To a good approximation, only the metal atoms are expected to contribute to the density modulation. A centrosymmetric model, consistent with the observed unit-cell size and symmetry is shown in Fig. 7(*b*). The model shown, model I, has maximum occupation at the origin. We may also consider a model, model II, which has minimum occupancy at the origin. Although the change of phase of the modulation does not affect the intensity of the satellite reflections, the two sinusoidal models lead to different ordered models as will be discussed below. Ideal atomic positions and occupancy factors for models I and II are given in Table 1. The sine function has been scaled in each case to give an overall fractional metal atom occupancy of the available octahedral sites of 0·6.* O atoms were not considered.

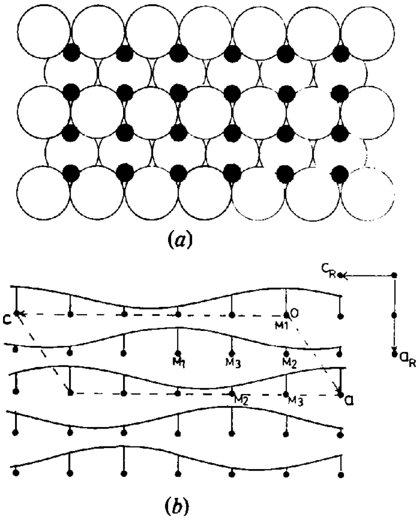
(*a*)

(*b*)

Fig. 7. (*a*) An $(020)_r$ section of hexagonal close-packed O atoms (open circles) showing all octahedral sites (as small filled circles). All sites occupied would conform to the NiAs structure. (*b*) $(020)_r$ metal atom sites only, shown as small filled circles, illustrating sinusoidal modulation of scattering power at octahedral sites along $[001]_r$, with a $5d(101)_r$ periodicity; maximum amplitude of modulation at the origin site. Between adjacent $(020)_r$ planes, the metals are displaced by $\frac{1}{2}[111]_r$.

The calculated $F^2$ values for the $(h0l)$ reflections for models I and II were identical and are shown in Fig. 6(*b*). Although the correct geometry of superlattice reflections was reproduced, the intensity distribution is

---

* In our previous structure study on an $(020)_r$ structure with an $11d(020)_r$ periodicity, the composition of this phase was determined to be $(Fe,Ti)O_{1{\cdot}929}$. From electron-imaging pictures such as those shown in Fig. 3, the number of metal atom layers most commonly encountered within the $(020)_r$ boundaries is two. Using this figure, the metal atom fraction in the intra-boundary structure is calculated to be 0·60.

quite different from that obtained experimentally, Fig. 6(*a*). We note that in model I, pairs of metal atoms $M(3)$, which occupy face-shared octahedral sites, have occupancy factors of 0·72 and are only 2·3 Å apart $[M(3)–M(3) = \frac{1}{2}a_r]$ and so considerable repulsion is expected for these metal atoms. They were each moved by ~0·25 Å towards the adjacent $M(2)$ sites which have average occupancies of only 0·28. This gives an $M(3)–M(3)$ separation across the shared face of 2·8 Å which is similar to the Fe—Fe separation across a shared octahedral face in haematite, $Fe_2O_3$. Using this new set of atomic coordinates, see Table 1, the ($h0l$) intensities were recalculated for model I. The resulting pattern is shown in Fig. 6(*c*). It is apparent that model I, with appropriate metal atom repulsion factors closely reproduces the observed diffraction pattern. (It can be shown that this model also gives a satisfactory fit to the upper level $[010]_r$ sections.) Comparable results were obtained for model II.

### 4.3. *Local atom-ordering models*

The sinusoidal modulation model is a mathematical approximation to the *average* metal atom ordering within a crystal. In the structures considered here, the metal atoms occupy octahedral sites in a close-packed O lattice and at the unit-cell level these octahedral interstices will be either filled or empty. Local atom ordering will involve specific sequences of the filled and empty sites. That the diffraction pattern can be reproduced with a sine-wave modulation of scattering power signifies that ordered arrangements of filled and empty sites occur over very small distances compared with the size of the crystal examined, and that no long-range order exists between the local atom-ordering domains. However, the amplitude of the modulation at any particular atom site should give a measure of the probability that the site will be filled or empty. Accordingly, we can construct models for the *most probable* local atom-ordering clusters by simply assigning sites with high modulation amplitudes as filled and those with low amplitudes as empty, at the same time ensuring that the distribution of filled and empty sites is compatible with the bulk composition. This approach gives a *physical* picture of the disordered structure, as comprising ordered arrangements or domains of metal atoms which are periodic over only a few unit cells, coherently intergrown, but with no regularity in the inter-domain periodicity.

The most probable local atom ordering for models I and II is given in Table 1 and shown in Fig. 8(*a*)–(*d*). For model I, this assignment was straightforward and unambiguous. However, for model II, the sinusoidal model has approximately one half occupancy of sites $M(3)$. The simplest ordered model consistent with the observed unit-cell symmetry has the sites $M(3)$ alternately all filled and all empty in successive $[001]_r$ rows. When this is done, and sites $M(1)$ and $M(2)$, with occupancies of 0·28 and 0·90, are considered empty and filled respectively, then model $II_{ord}$ obtains, Fig. 8(*c*)–(*d*). Corresponding layers of metal atoms in the rutile and corundum structures are shown in Fig. 9. It is seen that both models $I_{ord}$ and $II_{ord}$ comprise ordered intergrowths of corundum and rutile slabs, parallel to $(101)_r$.

Intensity calculations for both ordered models, using metal atoms only, and including metal atom repulsions across shared faces, are given in Fig. 6(*d*) and (*e*). Both patterns are in reasonable accord with the observed pattern. The $F$ centring of models $I_{sin}$ and $II_{sin}$ is reduced to $C$ centring only in model $II_{sin}$ and many more weak reflections appear in its ($h0l$) diffraction pattern; these reflections are marked with arrows in the experimental pattern, Fig. 6(*a*). However, the latter may also arise from O atom contributions, not considered in our simple treatment, or from structural distortions at the boundaries between the intergrowth slabs and rutile slabs. In each of these cases, the number of variables involved exceeds the number of

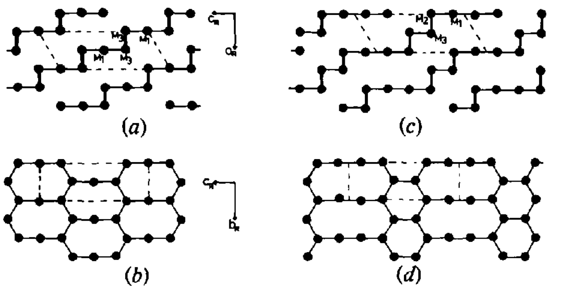

Fig. 8. (*a*) and (*b*) show single metal atom layers in the model $I_{ord}$ structure as viewed along $[010]_r$ and $[100]_r$ respectively. (*c*) and (*d*) show the corresponding sections for model $II_{ord}$. The metal atoms are represented by filled circles, the labels refer to the atoms given in Table 1. Light lines join atoms which share octahedral edges, and heavy lines join atoms which share octahedral faces. The unit cells are shown by dashed lines.

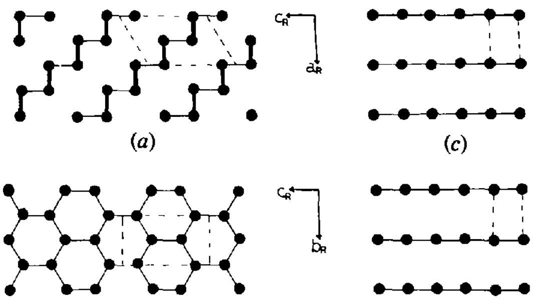

Fig. 9. (*a*) and (*b*) show single metal atom layers in corundum as viewed along $[010]_r$ and $[100]_r$ respectively. (*c*) and (*d*) show the corresponding sections for rutile. See Fig. 8 for explanation of symbols.

observed reflections and precludes structural refinements. Thus, in the absence of definitive experimental confirmation, the most that can be said is that both models $I_{ord}$ and $II_{ord}$ reproduce quite closely the observed distribution of strong, medium and weak intensities and support the general structural principle that the short-range ordering in the $(0kl)_r$ boundary slabs comprises rutile–corundum intergrowths parallel to $(101)_r$.

### 4.4. *Other intergrowth sequences*

The preceding discussion relates only to a model with a $5d(101)_r$ periodicity. However, the general structural principle of corundum–rutile intergrowth parallel to $(101)_r$ may be extended to describe other periodicities, simply by varying the proportions of the two components. Typical examples with 'average' periodicities of $4\cdot65d(101)_r$, $4\cdot50d(101)_r$ and $4d(101)_r$ are shown in Fig. 10. It is possible that the intergrowth periodicities may extend to lower values than $4d(101)_r$ by incorporating a larger corundum component, the lower limit being corundum itself, with a periodicity of $3d(101)_r$.

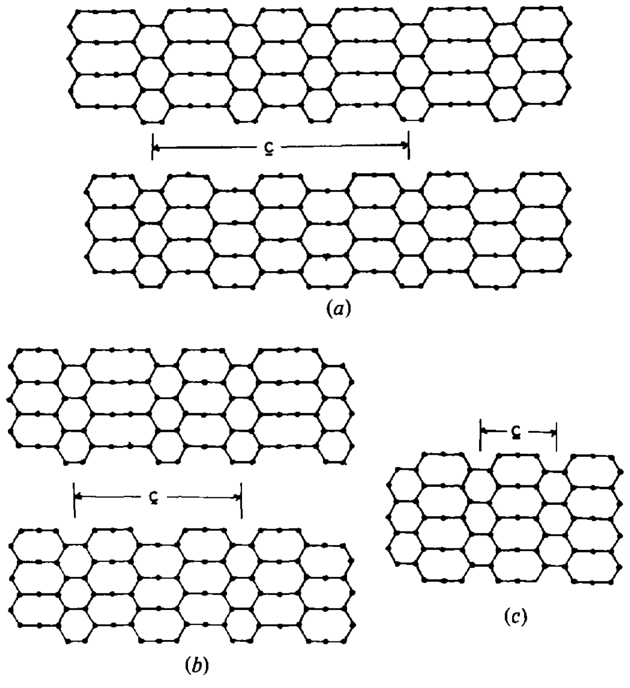

Fig. 10. Single layers of metal atoms, normal to $[100]_r$, in intra-boundary $(101)_r$ metal atom ordering models, with periodicities of (*a*) $14d(101)_r$, (*b*) $9d(101)_r$ and (*c*) $4d(101)_r$. In (*a*) and (*b*), two separate models with the same periodicity are shown; in each case the lower model comprises elements of model $I_{ord}$, intergrown with corundum whereas the upper model contains elements of both model $I_{ord}$ and model $II_{ord}$, intergrown with corundum. The available diffraction data do not allow an unambiguous assignment of one or the other of these alternatives.

The superlattice periodicities for the three examples shown in Fig. 10 are $14d(101)_r$, $9d(101)_r$ and $4d(101)_r$ respectively. The 'super-superlattice' reflections (Mann & Bevan, 1972) which define the long-range periodicities are very much weaker than the superlattice reflections, which define the average periodicities. Contributions from different intergrowth sequences (*i.e.* reflecting compositional inhomogeneity) tend to smear out these weaker contributions and we have never observed them in our preparations. In the absence of this experimental information, it is not possible to distinguish between alternative intergrowth models with the same overall periodicity, as shown for example, by the upper and lower models in Fig. 10(*a*) and (*b*). The presence of different intergrowth sequences in the same preparation also results in an enhancement of intensity of the superlattice reflections immediately adjacent to a subcell reflection, relative to reflections further away. This is illustrated in Fig. 11 where calculated intensities for an (001) row of reflections are shown for 4·67×, 4·50× and 4·33 × $(101)_r$ models. Also shown is a composite row representing equal contributions from all three models. This illustrates how the contributions to diffraction patterns from local atom-ordering sequences with slightly different periodicities can combine to give an apparent sinusoidal modulation pattern of intensities, Fig. 11(*e*).

### 4.5. *Complete structural models for high-temperature* $(020)_r$ *intergrowths*

In both the X-ray and electron diffraction patterns, diffuse streaks occurred, signifying a lack of correlation of the $(101)_r$ metal atom ordering between adjacent $(020)_r$ boundaries. Thus the space group cannot be unambiguously determined for these high-temperature, disordered structures. Without such definitive symmetry information, it is nevertheless possible to deduce a considerable amount of information about the complete structures from the available experimental data, bearing in mind that any ordered models will only occur over very limited regions (linear dimensions $\lesssim$50–100 Å) of the real crystals.

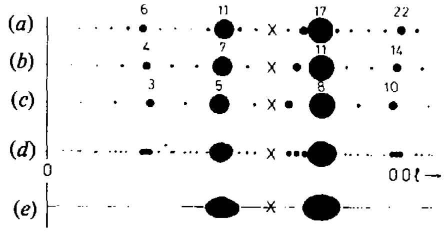

Fig. 11. Calculated $F^2$ values (areas of filled circles) for $(00l)$ lattice rows for intra-boundary $(101)_r$ metal ordering models with periodicities of (*a*) $14d(101)_r$, (*b*) $9d(101)_r$ and (*c*) $13d(101)_r$. (*d*) represents a composite row containing equal contributions from all three intergrowth structures, while (*e*) is an experimentally observed intensity pattern.

From previous structural study on an $(020)_r$ structure (Bursill, Grey & Lloyd, 1976), the above electron and X-ray diffraction data and the direct images obtained by electron microscopy, the following structural information is obtained. (i) The high-temperature phases comprise rutile slabs which are periodically displaced relative to one another by the vector $\frac{1}{2}[0\bar{1}1]_r$ across $(020)_r$ boundaries. (ii) Except for minor displacements, the O lattice is continuous across the boundaries. ($\frac{1}{2}[0\bar{1}1]_r$ is an O—O vector.) (iii) The boundaries are not single planes of atoms, as was assumed in the earlier structure analysis (Bursill, Grey & Lloyd, 1976), but have a finite width. (iv) Within the boundaries, the metal atom arrangement conforms to a rutile–corundum intergrowth, parallel to $(101)_r$. (v) To be consistent with the observed face-centring symmetry operation in the $(101)_r$ intergrowths, the boundary structure must comprise an even number of $(020)_r$ metal atom layers, corresponding to boundary thicknesses of 4·6 Å ($= b_r$), 9·2 Å, *etc.* The electron-microscope images and composition calculations are consistent with a double metal atom layer, 4·6 Å being the dominant contributor.

A proposed model for an ordered $(020)_r$ structure is shown in Fig. 12(*a*). It has an $11d(020)_r$ boundary separation, and a $5d(101)_r$ periodicity of rutile–corundum intergrowth within a boundary of width 4·6 Å. The metal atom occupancy of octahedral sites within a boundary is 0·6 and the overall composition is calculated as $(Fe,Ti)O_{1\cdot930}$. The calculated percentage by weight of $Fe_2O_3$ is 14·3, which is close to the observed upper compositional limit for the high-temperature intergrowth phases. Compositional variations in the $(020)_r$ structures may be accommodated by varying the average $(020)_r$ boundary separation, by changing the intergrowth sequence of corundum and rutile within the boundary and by varying the width of the boundary. The available diffraction and electron-image data indicate that considerable variations in all three occur.

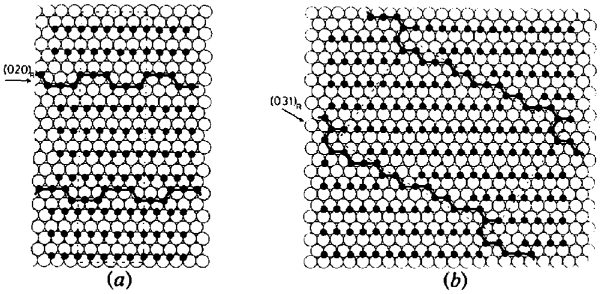

Fig. 12. (*a*) Proposed model for an $(020)_r$ high-temperature intergrowth structure of composition $(Fe,Ti)O_{1\cdot930}$, viewed down $[100]_r$. The intra-boundary metal atom ordering has a $5d(101)_r$ periodicity (model $I_{ord}$) and the average $(020)_r$ intergrowth periodicity is $11d(020)_r$. (*b*) Proposed model for an $(031)_r$ high-temperature intergrowth structure of composition $(Fe,Ti)O_{1\cdot949}$, viewed down $[100]_r$. The intra-boundary metal atom ordering has a $4d(101)_r$ periodicity.

As the $Fe_2O_3$ content is lowered, a fourth method of accommodating composition change is introduced, *i.e.* change in orientation of the boundaries. For different preparations in the $Fe_2O_3$–$TiO_2$ system, we have observed that $(0kl)_r$ orientations between $(020)_r$ and $(031)_r$ occur (Bursill, Grey & Lloyd, 1976). In the $Cr_2O_3$–$TiO_2$ system, we find that the boundary orientation swings even further, towards $(021)_r$, *i.e.* in each case the indices of the boundary lie in the $[100]_r$ zone. Proposed models for the $(0kl)$ structures are discussed below.

### 4.6. $(0kl)_r$ *intergrowths*

Irrespective of the $(0kl)_r$ boundary orientation, it was observed that the diffraction pattern of diffuse reflections from the intra-boundary ordering remained qualitatively the same; *i.e.* the centres of the diffuse streaks maintained their positions on superlattice rows along $\mathbf{g}(101)_r$. With changing orientation, only the directions of the streaks changed, and these were always along $\mathbf{g}(0kl)$. Thus, any $(0kl)_r$ intra-boundary structure should be obtainable simply by taking the appropriately orientated slice from the three-dimensional $(101)_r$ rutile–corundum intergrowth model with correct $d(101)_r$ periodicity. [Examples of these extended three-dimensional models for different $d(101)_r$ periodicities are shown in Fig. 10.] A proposed model for an $(031)_r$ intergrowth structure is shown in Fig. 12(*b*). The $(031)_r$ boundaries are separated by 28·2 Å and the $(101)_r$ intra-boundary metal ordering has a periodicity of $4d(101)_r$, *i.e.* an $(031)_r$ slice of the rutile–corundum intergrowth structure shown in Fig. 10(*c*) was used. The composition is calculated to be $(Fe,Ti)O_{1\cdot949}$, corresponding to an $Fe_2O_3$ content of 10·2 wt%.

Using these principles, it is possible to predict high-temperature structures with any observed combination of inter-boundary spacing, orientation and intra-boundary ordering periodicity. Only a complete structure refinement on an $(0kl)_r$ structure, incorporating both sharp and diffuse diffraction effects, will determine if the details of the models, as shown in Fig. 12, are completely correct. This is not contemplated at this stage.

### 4.7. *Structure decomposition in the electron beam*

The effect of electron-beam heating on the intra-boundary ordering in an $(020)_r$ structure is illustrated in Fig. 2. In Fig. 2(*a*), at the beginning of the experiment, $\mathbf{g}(101)_r$ superlattice reflections with approximately $5d(101)_r$ periodicity are observed. Fig. 2(*b*) shows the formation of new $\mathbf{g}(101)_r$ reflections, with a periodicity corresponding to $3d(101)_r$. Finally, in Fig. 2(*c*) and (*d*), only the latter superlattice reflections are observed. A bright-field image corresponding to the situation shown in Fig. 2(*d*) is shown in Fig. 4. It may be interpreted as comprising lenses of haematite, $Fe_2O_3$, within a matrix of rutile. Haematite has the corundum structure, with a $d(101)_h$ repeat of 7·5 Å ≡ $3d(101)_r$. The haematite lenses remain approximately parallel to $(020)_r$, *i.e.* it appears that the high-temperature intra-boundary $(101)_r$ corundum–rutile intergrowth structures are metastable at low temperatures and beam heating causes a breakdown into the component oxides.

## 5. Discussion

### 5.1. *Relation between* $(101)_r$ *intergrowths and pseudorutile*

The $5d(101)_r$ model proposed for intra-boundary short-range order, model $\mathrm{I}_{\mathrm{ord}}$ in Fig. 8(*a*) and (*b*), has an interesting analogue in the ferric titanate mineral, pseudorutile, $Fe_2Ti_3O_9$. This mineral is an alteration product of ilmenite, $FeTiO_3$, and derives from the oxidation of the ferrous iron to the ferric state, together with leaching of one third of the Fe and rearrangement of the remaining Fe and Ti among the octahedral sites within the hexagonally close-packed O lattice. As with the high-temperature phases reported here, pseudorutile also shows only short-range order of the metal atoms and the metal ordering reflections are very diffuse. A model for the short-range-order clusters of pseudorutile, consistent with the observed single-crystal diffraction effects (Grey & Reid, 1975) is reproduced in Fig. 13, which shows an $(001)_{\mathrm{p.r.}}$ (p.r. = pseudorutile) layer of metals. It is apparent that pseudorutile contains the same short-range-order clusters of octahedra as those in model $\mathrm{I}_{\mathrm{ord}}$. However, in pseudorutile, these clusters (*i.e.* the eight-membered rings of octahedra as outlined in Fig. 13) are in a triply twinned orientation. This is a consequence of the topotaxic growth of pseudorutile on remaining unaltered ilmenite, where the trigonal symmetry of the ilmenite dictates the structure growth of the pseudorutile. Both structures are metastable at low temperatures; as demonstrated in the above sections, the high-temperature intergrowths decompose under electron-beam heating to give haematite and rutile and heating pseudorutile above 200 °C causes a transformation to an ordered $V_3O_5$–α-$PbO_2$-type intergrowth (Grey, Reid & Allpress, 1973) with the same composition, $Fe_2Ti_3O_9$.

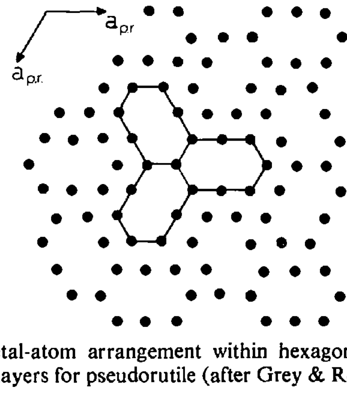

Fig. 13. Metal-atom arrangement within hexagonal close-packed anion layers for pseudorutile (after Grey & Reid, 1976).

### 5.2 *Low-temperature–high-temperature structure transformation*

As discussed previously (Bursill, Grey & Lloyd, 1976), the high-temperature intergrowths in the $Fe_2O_3$–$TiO_2$ system result from a reversible order–disorder transformation, where the ordered, low-temperature precursors are the well known $(121)_r$–$(132)_r$ 'swinging-shear', rutile-derived CS structures. The transformation involves a cooperative reorientation of the CS planes, from the $[1\bar{1}1]_r$ zone to the $[100]_r$ zone, while the CS plane spacing remains almost constant. The present study shows that the nature of the metal ordering within the CS boundaries changes significantly during the transformation. The structure of a $(121)_r$ CS boundary is represented in Fig. 14(*a*). It consists of corundum-like chains of edge- and face-shared octahedra along $[1\bar{1}1]_r$. These link, forming $(121)_r$ planes *via* octahedra corner-sharing along $[10\bar{1}]_r$. If the corundum structure is viewed along this projection (*i.e.* $[010]_r$), Fig. 14(*b*), it is seen to comprise identical $[10\bar{1}]$ strings of corner-linked octahedral pairs, but these link to form $(020)_r$ planes *via* octahedral edge-sharing along $[102]_r$. The corresponding view of the $(101)_r$ corundum–rutile intergrowth with composition $M_3O_5$, is shown in Fig. 14(*c*). Finally, in Fig. 14(*d*), the $(101)_r$ corundum part of the intergrowth is

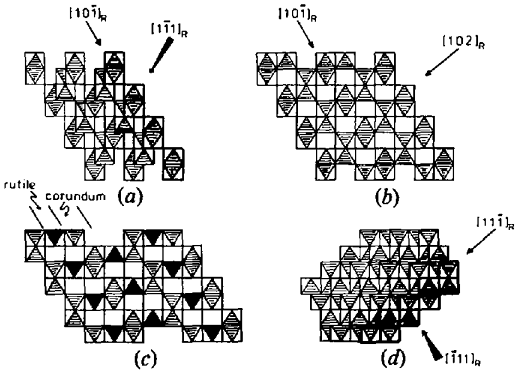

Fig. 14. (*a*) Articulation of octahedra within a $(121)_r$ CS plane, as viewed along $[010]_r$, showing face-shared pairs of octahedra joined by edges into chains along $[1\bar{1}1]_r$ and by corners into chains along $[10\bar{1}]_r$. (*b*) Equivalent view of a layer of octahedra in corundum. (*c*) An $[010]_r$ view of an octahedral layer in the intra-boundary metal ordering model, model $\mathrm{I}_{\mathrm{ord}}$, *i.e.* a 1:1 intergrowth of corundum and rutile, parallel to $(10\bar{1})_r$. (*d*) A $(101)_r$ slice of the corundum structure, viewed along $[012]_r$.

viewed along $[012]_r$. It is seen that it comprises two interpenetrating sets of $\langle 111 \rangle$ strings of edge-linked octahedral face-shared dimers, the directions of both strings being different from that in the low-temperature $(121)_r$ precursor phase, Fig. 14(*a*). In transforming to the high-temperature phases, the integrity of the $[1\bar{1}1]_r$ strings is lost, but the $[10\bar{1}]_r$ strings of corner-linked face-shared octahedral pairs persist.

A high-resolution electron-imaging and diffraction study of the transformation mechanism has been carried out and will be reported elsewhere (Bursill & Grey, 1977). This study shows $(121)_r$ and $(\bar{1}2\bar{1})_r$ CS structures intersecting to form $(101)_r$ interfaces containing the $[10\bar{1}]_r$ strings common to both high- and low-temperature structures. These $[10\bar{1}]_r$ structural features (imaged edge-on in Figs. 3 and 4) provide the key to the structural relations and the reaction mechanism. It is interesting to note that the high-temperature structures may be derived mathematically as follows:

$$\text{I} \quad (020)_r = (121)_r + (\bar{1}2\bar{1})_r,$$

$$\text{II} \quad (0kl)_r = p(020)_r + q(011)_r.$$

The element $(011)_r$ represents the same anti-phase component required for swinging in the low-temperature structures.

Part of this work was supported by the Australian Research Grants Committee. The authors express their gratitude to Mr M. Brown of Melbourne University Physics Department for preparation of the electron diffraction photographs.

### References

Andersson, S., Sundholm, A. & Magnéli, A. (1959). *Acta Chem. Scand.* **13**, 989–997.

Bursill, L. A. (1974). *J. Solid State Chem.* **10**, 72–94.

Bursill, L. A. & Grey, I. E. (1977). Am. Crystallogr. Assoc. Summer Meet. Program Abstr. Ser. 2, Vol. 5, No. 2, Abstr. E5.

Bursill, L. A., Grey, I. E. & Lloyd, D. J. (1976). *J. Solid State Chem.* **16**, 331–347.

Flörke, O. W. & Lee, C. W. (1970). *J. Solid State Chem.* **1**, 445–453.

Grey, I. E. & Reid, A. F. (1975). *Am. Mineral.* **60**, 898–906.

Grey, I. E., Reid, A. F. & Allpress, J. G. (1973). *J. Solid State Chem.* **8**, 86–99.

Mann, A. W. & Bevan, D. J. M. (1972). *J. Solid State Chem.* **5**, 410–418.

---

*Acta Cryst.* (1978). B**34**, 2424–2428

# Hydrogen Bond Studies.

# CXXIX.* An X-ray Determination of the Crystal Structure of Hydrogen Chloride Hexahydrate, $H_9O_4^+Cl^-.2H_2O$

By Inger Taesler and Jan-Olof Lundgren

*Institute of Chemistry, University of Uppsala, Box* 531, *S*-751 21 *Uppsala, Sweden*

(*Received* 24 *January* 1978; *accepted* 21 *March* 1978)

The structure of hydrogen chloride hexahydrate has been determined by X-ray diffraction at 87 K. The crystal is orthorhombic, space group *Pbcm*, $a = 6{\cdot}3302$ (1), $b = 6{\cdot}4528$ (1), $c = 17{\cdot}8979$ (3) Å, $Z = 4$. The structure contains $H_9O_4^+$ ions and water molecules hydrogen-bonded to each other and to $Cl^-$ ions to form a layer structure. O–H···O hydrogen bonds within the $H_9O_4^+$ complex are 2·514 (1), 2·514 (1) and 2·540 (2) Å. Other O–H···O bonds are 2·753 (1) and 2·805 (1) Å.

## Introduction

This report is part of a systematic study of the hydrated proton in solids in progress at this Institute. The study of the hexahydrate of hydrogen chloride is of special interest since its composition gives the possibility of the formation of an $H_{13}O_6^+$ ion.

The freezing-point diagram of the system hydrogen chloride/water (Pickering, 1893; Rupert, 1909) indicates the existence of the mono-, di- and trihydrates of HCl. The existence of the hexahydrate was later shown by Vuillard (1955). $HCl.6H_2O$ melts congruently at −70·0 °C.

The monohydrate (Yoon & Carpenter, 1959) was found to contain the oxonium ion, $H_3O^+$, whereas crystals of the di- and trihydrates both contain the

---

* Part CXXVIII: Loehlin & Kvick (1978).